

Constraints on the Magnetic Field Strength of HAT-P-7 b and other Hot Giant Exoplanets

T.M. Rogers^{1,2}

¹ Department of Mathematics & Statistics, Newcastle University, UK

² Planetary Science Institute, Tucson, AZ, 85721, USA

SUMMARY

Observations of infrared and optical light curves of hot Jupiters have demonstrated that the peak brightness is generally offset eastward from the substellar point [1,2]. This observation is consistent with hydrodynamic numerical simulations that produce fast, eastward directed winds which advect the hottest point in the atmosphere eastward of the substellar point [3,4]. However, recent continuous Kepler measurements of HAT-P-7 b show that its peak brightness offset varies significantly in time, with excursions such that the brightest point is sometimes westward of the substellar point [5]. These variations in brightness offset require wind variability, with or without the presence of clouds. While such wind variability has not been seen in hydrodynamic simulations of hot Jupiter atmospheres, it has been seen in magnetohydrodynamic (MHD) simulations [6]. Here we show that MHD simulations of HAT-P-7 b indeed display variable winds and corresponding variability in the position of the hottest point in the atmosphere. Assuming the observed variability in HAT-P-7 b is due to magnetism we constrain its minimum magnetic field strength to be 6 G. Similar observations of wind variability on hot giant exoplanets, or lack thereof, could help constrain their magnetic field strengths. Since dynamo simulations of these planets do not exist and theoretical scaling relations [7] may not apply, such observational constraints could prove immensely useful.

MAIN TEXT

To demonstrate magnetic effects on the winds of HAT-P-7 b, we simulate the atmosphere of a hot giant exoplanet with parameters similar to HAT-P-7 b using a spherical, three-dimensional (3D), anelastic MHD code [8,6]. We start with a hydrodynamic simulation of HD209458 b in terms of gravity, radius and rotation, but with a mean temperature (2200K) and temperature differential (1000K) of HAT-P-7 b (temperature and magnetic diffusivity profiles are shown in Supplementary Figure 1). The strong day-night temperature differential drives strong eastward atmospheric winds, consistent with previous simulations [9,10]. This simulation is run for ~ 100 rotation periods before a magnetic field is added after which both the hydrodynamic and MHD simulations are run for an additional 280 rotation periods. Details of the numerical code and simulation can be found in the Methods section.

The extreme temperatures of HAT-P-7 b give rise to significant thermal ionization of alkali metals [11,12], which leads to coupling of the atmosphere to the deep seated magnetic field [13] and could also lead to an atmospheric dy-

namo [14]. The Lorentz force arising from this magnetic interaction disrupts the strong eastward directed atmospheric winds typically seen in hydrodynamic simulations, leading to variable and even oppositely directed winds [6]. Figure 1 shows a time-snapshot of magnetic field lines in the simulation looking onto the eastside terminator (a corresponding video of its complex evolution and variability is available in the Supplementary Material). The zonal-mean zonal-wind, averaged within 17° of the equator and over the upper 1 mbar of the simulated domain, as a function of time is shown in Figure 2, along with the position of the hottest point in the atmosphere (also determined by an average over the same latitudes and height). There we see that, the hydrodynamic model retains a strong, eastward jet and associated positive hotspot displacement throughout the simulation (dotted line in Figure 2a and 2b). When a magnetic field is added, the zonal winds slow dramatically, reverse and then settle into an oscillatory pattern, with a timescale of $\sim 10^6$ s, consistent with the Alfvén time ($\tau_A = \sqrt{4\pi\rho\lambda}/B$) of the imposed 10 G field and is of the same order as the timescale of variability observed in HAT-P-7 b [5]. Variability in the hot spot displacement, including negative offsets, is seen on a similar timescale.

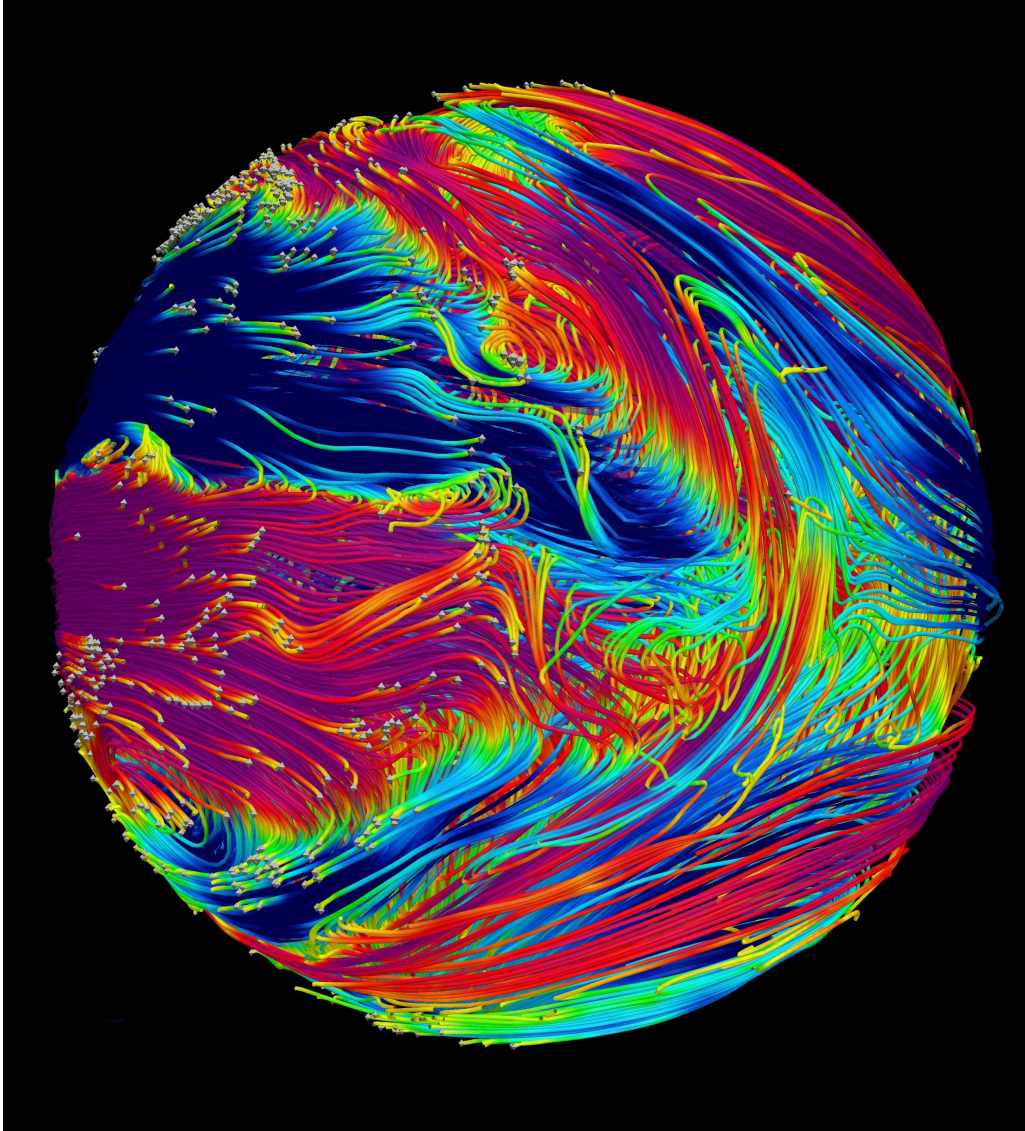


Figure 1: Magnetic Field lines in the atmosphere of a Hot Giant Exoplanet. Time snapshot of magnetic field lines in the numerical simulation of a hot Jupiter atmosphere (a model of HD209458 b but with a temperature structure similar to HAT-P-7 b). Magnetic field lines are color-coded to represent the azimuthal (toroidal) magnetic field with blue representing negative directed field (saturated at -50 G) and magenta positive (saturated at 50 G), with green and yellow ranging from -5 G to 5 G, respectively. The vantage point is looking onto the east-side terminator.

Both the hydrodynamic and MHD models have more positive hot-spot displacements than the observations. This is expected given that the waves that force super-rotation can propagate further in HD209458 b than HAT-P-7 b before being damped [15]. Therefore, we expect a hydrodynamic model with HAT-P-7 b's gravity and rotation rate would show reduced hot-spot displacements compared to HD209458

b and we indeed find this (see Figure 3). While this magnetic model has some uncertainties (enhanced viscosity, crude radiative transfer), it naturally explains the bright spot excursions as due to changes in the thermal structure of the planet caused by variable winds. In this model clouds may not be necessary as HAT-P-7 b is hot enough that even the optical signal could be dominated by thermal emission. Moreover, this

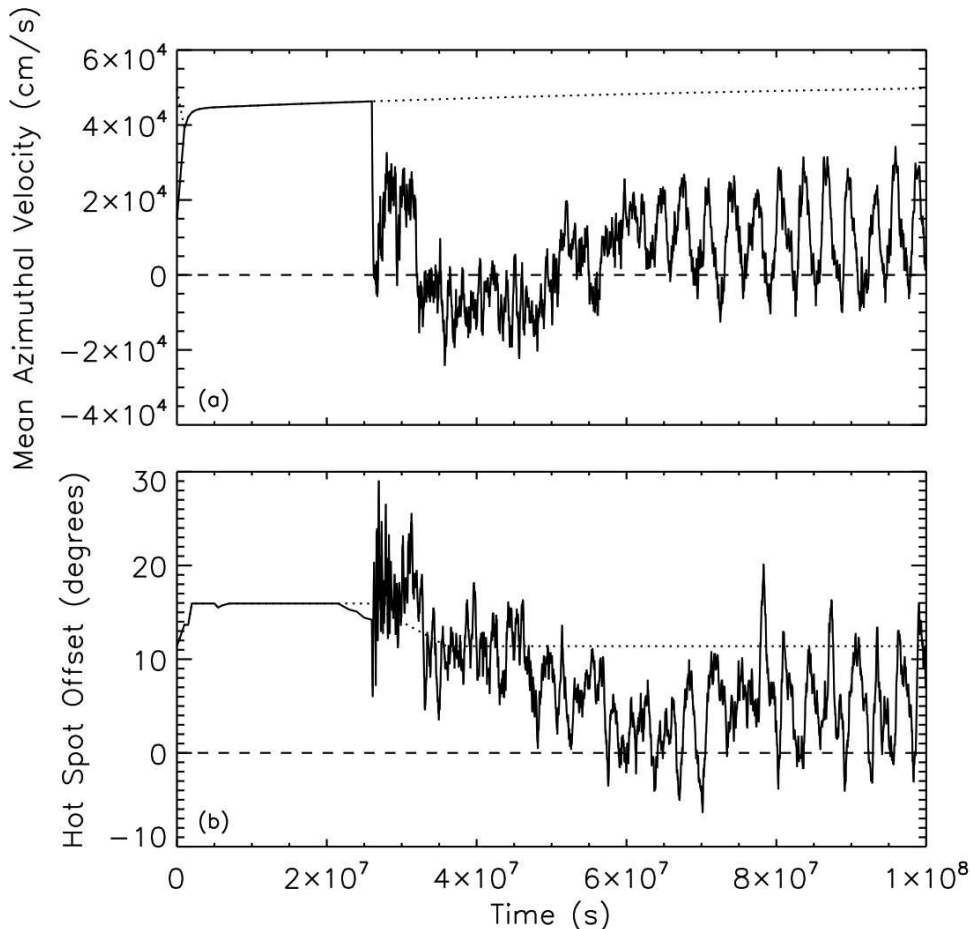


Figure 2: Atmospheric Dynamics of Simulated Hot Giant Exoplanet.] (a) Zonal Mean Zonal Wind in the hot Jupiter atmosphere averaged over 17° around the equator and over the upper 1 mbar of the simulated domain. Dotted line shows the winds in the hydrodynamic model while the solid line shows the winds in the MHD model. (b) Displacement of the hottest point of the atmosphere from the substellar point, at the same location and averaged as in (a). Similar to the mean winds, the hot-spot displacement in the MHD model (solid line) shows strong variability with excursions to points west of the substellar point. Hydrodynamic models show a stable, positive offset.

model may also explain the timescale of the observed fluctuations as due to Alfvén waves. At the very least, it can provide the wind variability needed for models requiring clouds [5].

The effect of magnetism on zonal winds depends on the ratio of the magnetic to inertial terms in the momentum equation, which can be approximated as the ratio of magnetic to wave timescales τ_{mag}/τ_{wave} , where $\tau_{mag} = 4\pi\rho\eta/B^2$ and $\tau_{wave} = L/\sqrt{gH}$. Here ρ is the density, η is the magnetic diffusivity, B is the magnetic field strength, g is the gravity, L is the characteristic length scale of the horizontal flow and H is the depth of the atmosphere [11,15]. As magnetic effects are increased, either through increased magnetic field strength or increased conductiv-

ity, their effect on atmospheric zonal winds progressed from little to no effect (when $\tau_{mag} > \tau_{wave}$), to oscillatory winds (when $\tau_{mag} \sim \tau_{wave}$) to completely reversed (westward) winds (when $\tau_{mag} < \tau_{wave}$) [6]. Assuming the variable winds observed on HAT-P-7 b are due to magnetism and applying the oscillatory wind condition we find $B \sim \sqrt{4\pi\eta\rho/\tau_{wave}}$. Using the nightside value of η , we find that HAT-P-7 b must have a minimum field strength of ~ 6 G. This value is consistent with the theoretical scaling relation based on the Elsasser number [16] ($\Lambda = 2\rho\Omega/\mu_0\eta \sim 1$) and with the upper limit placed on WASP-12 b [17], if we were to assume it had a similar field strength.

To check this constraint, we ran additional

models of HAT-P-7 b, with the appropriate rotation, gravity, size and temperature [18]. The temperature and magnetic diffusivity profiles for this model can be seen in Supplementary Figure 2. After running a hydrodynamic model for 140 rotation periods a magnetic field was added and run an additional 15 rotation periods. We show the hot spot displacement for those models in Figure 3. We see that the hydrodynamic model (black line) has a steady hot-spot displacement of 2.8° . The MHD model with a 3 G field (red line) shows a similar, stable hot spot displacement. However, both the 10 G (blue line) and 20 G (orange line) model show wind variability ranging from $\sim -15^\circ$ – 20° . This range of displacement is more consistent with brightness variations observed (which range from $\sim -25^\circ$ – 25°). However, clouds could also play a role in enhancing the large displacements observed by Kepler [5].

In our simulations wind variability sets in between 3 and 10 G, consistent with the 6 G lower limit based purely on a simple timescale analysis. If we had used the dayside magnetic diffusivity in the estimate the lower limit would have been ~ 0.6 G, inconsistent with our follow up models, which show no variability at 3 G. This estimate depends only on the winds being variable and is independent of whether or not clouds are needed to explain the exact range of variability seen. Although these models are consistent with the 6 G lower limit, on this timescale we see no completely reversed winds and therefore, conclude that we can only place a *lower* limit on the field strength. While it may be possible to hone this constraint with more simulations, its likely not worthwhile given the other limitations of these

simulations.

The continuous observations of HAT-P-7 b [5] were unique in that previous optical and infrared observations have generally only provided this measurement at a single epoch. The exception is the multiple epoch Spitzer observations of HD189733 b [19]. That work showed a fairly stable, positive offset. This lack of variability is consistent with little or no magnetic effects in HD189733 b, a plausible conclusion given that the low temperatures of HD189733 b would require unrealistic magnetic field strengths of ~ 100 – 1000 G to cause variability. In general, we would expect to see wind variability in objects where field-flow coupling is strong (as measured by the ratio of magnetic and wave timescales). Therefore, we would predict variability may also be found in other hot giant exoplanets, such as WASP-19b or WASP-12b.

While long timeline or multiple epoch observations of hot Jupiters' phase curves have not been carried out for many objects, such a campaign coupled with MHD models of those planets' atmospheres could be used to place constraints on the magnetic field strengths of hot Jupiters. Such constraints are rare [20] and would be useful for dynamo theory, planetary evolution and interpretations of star-planet magnetic interactions [17]. As recently shown [5], these types of constraints are already possible with Kepler but will become more readily available with upcoming space missions such as JWST, CHEOPS, TESS and PLATO. In particular, JWST will be able to measure infrared phase curves directly, thus testing this theory without the complication clouds might add to optical curves.

ADDENDUM

ACKNOWLEDGMENTS

T. R. thanks J. N. McElwaine, and G. Glatzmaier for helpful discussions leading to this manuscript and J. Vriesema for help with the graphics. Funding for this work was provided by NASA grant NNX13AG80G and computing was carried out on Pleiades at NASA Ames.

AUTHOR CONTRIBUTIONS

T.R. carried out all work related to this manuscript.

REQUESTS AND CORRESPONDENCE

Correspondence and requests for materials should be addressed to T. M. Rogers
tamara.rogers@newcastle.ac.uk

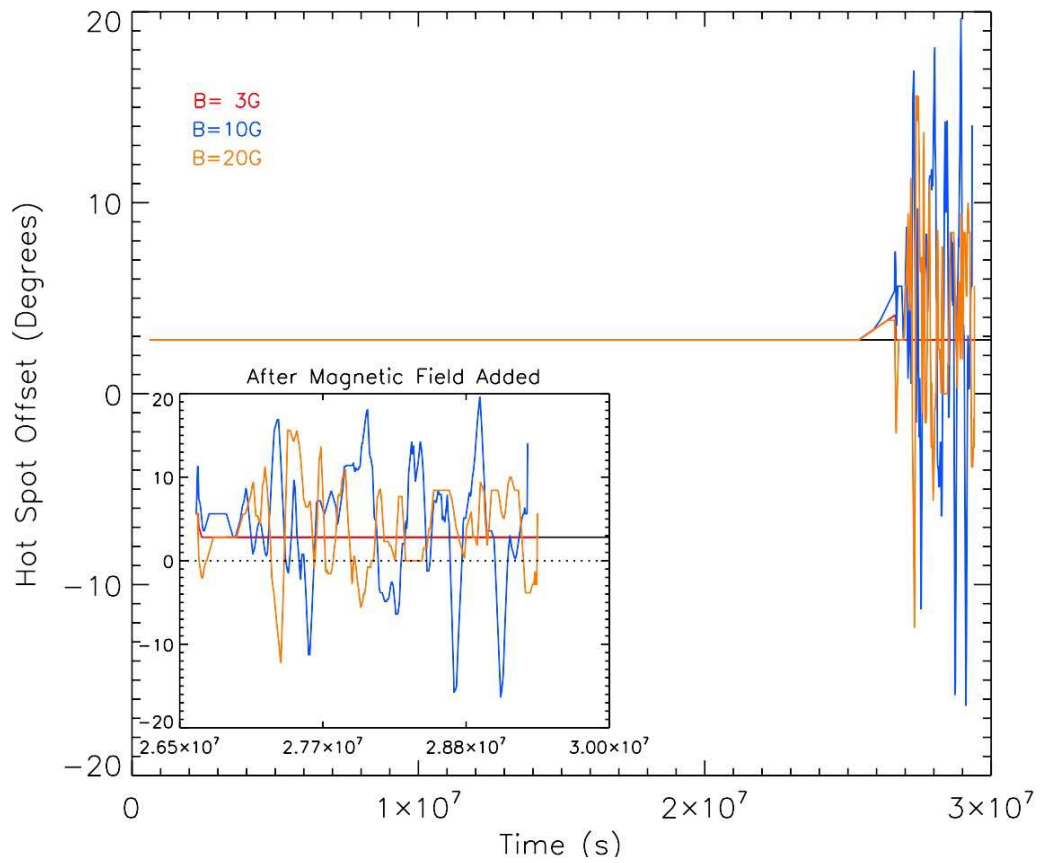


Figure 3: Hot spot displacement of Simulated HAT-P-7b.] Hottest point in the atmosphere, calculated after a latitudinal average around 17° of the equator and the upper 1mBar of the simulated domain, as a function of time. Black line shows the hydrodynamic model (barely visible under the other lines), red line is for a 3 G field, blue line is for a 10G field and orange line is for a 20 G field. The dotted line shows the sub-stellar point. The inset shows the time behavior after the magnetic field is added.

METHODS

We solve the magnetohydrodynamic (MHD) equations in three-dimensional (3D), spherical geometry in the anelastic approximation[6]. The model solves the following equations:

$$\nabla \cdot (\bar{\rho}\mathbf{v}) = 0 \quad (1)$$

$$\nabla \cdot \mathbf{B} = 0 \quad (2)$$

$$\bar{\rho} \frac{\partial \mathbf{v}}{\partial t} + \nabla \cdot (\bar{\rho}\mathbf{v}\mathbf{v}) = -\nabla p - \rho \bar{g} \hat{\mathbf{r}} \quad (3)$$

$$+ 2\bar{\rho}\mathbf{v} \times \boldsymbol{\Omega} + \nabla \cdot \left[2\bar{\rho}\bar{v} \left(E - \frac{1}{3}(\nabla \cdot \mathbf{v})\mathbf{1} \right) \right] + \frac{1}{\mu_0}(\nabla \times \mathbf{B}) \times \mathbf{B}$$

$$\frac{\partial T}{\partial t} + (\mathbf{v} \cdot \nabla)T = -v_r \left[\frac{\partial \bar{T}}{\partial r} - (\gamma - 1)\bar{T}h_\rho \right] + (\gamma - 1)Th_\rho v_r + \quad (4)$$

$$\gamma \bar{\kappa} \left[\nabla^2 T + (h_\rho + h_\kappa) \frac{\partial T}{\partial r} \right] + \frac{T_{eq} - T}{\tau_{rad}} + \frac{\eta}{\mu_0 \rho c_p} |\nabla \times \mathbf{B}|^2$$

Equation (1) represents the continuity equation in the anelastic approximation [21,22]. This approximation allows some level of compressibility by allowing variation of the reference state density, $\bar{\rho}$, which varies in this model by four orders of magnitude. Equation (2) represents the conservation of magnetic flux. Equation (3) represents conservation of momentum including Coriolis and Lorentz forces. Equation (4) represents the energy equation including a forcing term to mimic stellar insolation (fourth term on right hand side, where T_{eq} is the equilibrium temperature) and Ohmic heating (fifth term on right hand side). The radiative timescale in the Newtonian forcing term, τ_{rad} is a function that varies between 10^4 s at the outermost layers 10^6 s at the lowest layers. All other variables take their usual meaning [6].

The magnetic diffusivity η (inverse conductivity) is a function of all space. If we separate the magnetic diffusivity into a mean ($\bar{\eta}$) and fluctuating (η') component:

$$\eta(r, \theta, \phi) = \bar{\eta}(r) + \eta'(r, \theta, \phi) \quad (5)$$

where r , θ and ϕ are the radius, colatitude and longitude, respectively. The magnetic induction equation becomes

$$\frac{\partial \mathbf{B}}{\partial t} = \nabla \times (\mathbf{v} \times \mathbf{B} - \eta' \nabla \times \mathbf{B}) - \nabla \times (\bar{\eta} \nabla \times \mathbf{B}) \quad (6)$$

Equation (6) is solved along with Equations (1)-(4).

The magnetic diffusivity (5) is calculated from the initial temperature profile given by:

$$T_{eq}(r, \theta, \phi) = \bar{T}(r) + \Delta T_{eq}(r) \cos \theta \cos \phi \quad (7)$$

where $\bar{T}(r)$ is mean reference state temperature and ΔT_{eq} is the specified day-night temperature difference, here set to 1000K and which is extrapolated logarithmically from the surface to 10 bar. Using this temperature profile, the magnetic diffusivity is calculated as[23]:

$$\eta(r, \theta, \phi) = 230 \frac{\sqrt{T}}{\chi_e} \quad (8)$$

and χ_e is the ionization fraction. The ionization fraction is calculated at each point using a form of the Saha equation taking into account all elements from hydrogen to nickel and typical elemental abundances[24].

The model presented in Figure 1 and 2 is the model for HD209458 b [25] with 800K added at each vertical level and with an imposed day-night temperature variation of 1000K. The rotation rate, radius and gravity are all that of HD209458 b. The temperature and diffusivity profiles of this model are shown in Supplementary Figure 1. While this model is clearly not HAT-P-7 b it has a temperature (and thus, conductivity) structure similar to that expected for HAT-P-7 b. Since it is the temperature (conductivity) structure that dominates the MHD behavior of the atmosphere,

this model is probably a faithful, albeit imperfect, representation of the atmospheric dynamics in HAT-P-7 b. The model has 10G poloidal field imposed at the bottom boundary.

The model presented in Figure 3 is a model of HAT-P-7 b using an atmosphere model for HAT-P-7 b [18]. The temperature and magnetic diffusivity profiles can be seen in Supplementary Figure 2. Here, dipole fields of 3G, 10G and 20 G are imposed at the bottom boundary to mimic the deep seated dynamo field.

Both the models presented have more complex dynamics than those found previously [26,6] because these include a magnetic diffusivity (conductivity) that is a function of all space. This led to more complex field-flow interactions, particularly at the terminators (both) and even led to an atmospheric dynamo [14]. Although it was not included here a time-dependent conductivity could further complicate matters, particularly with regard to the thermal structure of the atmosphere. Currently, we see more Ohmic heating on the night side of the planet, which leads to reduction of the day-night temperature gradient. Naively, if we allowed this to react back on the flow and conductivity we would expect decreased wind driving and increased field-flow coupling. That is, we might expect wind variability at even lower magnetic field strengths.

DATA AVAILABILITY STATEMENT The data that support the plots within this paper and other findings of this study are available from the corresponding author upon reasonable request.

REFERENCES

- [1] Knutson, H. A. *et al.* Multiwavelength Constraints on the Day-Night Circulation Patterns of HD 189733b. *Astrophys. J.* **690**, 822–836 (2009).
- [2] Wong, I. *et al.* 3.6 and 4.5 μm *spitzer* phase curves of ten highly-irradiated hot jupiters wasp-19b and hat-p-7b. *Astrophys. J.* **680**, 83–122 (2016).
- [3] Showman, A. P. & Guillot, T. Atmospheric circulation and tides of “51 Pegasus b-like” planets. *Astron. Astrophys.* **385**, 166–180 (2002).
- [4] Dobbs-Dixon, I. & Lin, D. N. C. Atmospheric Dynamics of Short-Period Extrasolar Gas Giant Planets. I. Dependence of Nightside Temperature on Opacity. *Astrophys. J.* **673**, 513–525 (2008).
- [5] Armstrong, D. *et al.* Variability in the atmosphere of the hot giant planet hat-p-7b. *Nature Astronomy* **1** (2016).
- [6] Rogers, T. M. & Komacek, T. Magnetic Effects in hot Jupiter Atmospheres. *Astrophys. J.* **794**, 132–144 (2014).
- [7] Christensen, U. Dynamo scaling laws and applications to the planets. *Space Sci Rev* **152**, 565–590 (2010).
- [8] Rogers, T. M. On Limiting the Thickness of the Solar Tachocline. *Astrophys. J.* **733**, 12–25 (2011).
- [9] Cooper, C. S. & Showman, A. P. Dynamic Meteorology at the Photosphere of HD 209458b. *Audio, Transactions of the IRE Professional Group on* – (2005).
- [10] Rauscher, E. & Menou, K. Three-dimensional Modeling of Hot Jupiter Atmospheric Flows. *Astrophys. J.* **714**, 1334–1342 (2010).
- [11] Perna, R., Menou, K. & Rauscher, E. Magnetic drag on hot jupiter atmospheric winds. *Astrophys. J.* **719**, 1421–1426 (2010).
- [12] Batygin, K. & Stevenson, D. J. Inflating Hot Jupiters with Ohmic Dissipation. *Astrophys. J. Lett.* **714**, L238–L243 (2010).
- [13] Menou, K. Magnetic Scaling Laws for the Atmospheres of Hot Giant Exoplanets. *Astrophys. J.* **745**, 138–146 (2012).

- [14] Rogers, T. & McElwaine, J. The hottest hot-jupiters may host atmospheric dynamos. *Astrophys. J. Lett.* (submitted, 12/2016).
- [15] Perez-Becker, D. & Showman, A. P. Atmospheric Heat Redistribution on Hot Jupiters. *Astrophys. J.* **776**, 134–150 (2013).
- [16] Stevenson, D. Turbulent thermal convection in the presence of rotation and a magnetic field — A heuristic theory. *Geophys Astro Fluid* **12**, 139–169 (1979).
- [17] Vidotto, A., Jardine, M. & Helling, C. Early UV Ingress in WASP-12b: Measuring Planetary Magnetic Fields. *Astrophys. J. Lett.* **722**, 168–172 (2010).
- [18] Barman, T. S., Hauschildt, P. H. & Allard, F. Phase-dependent properties of extrasolar planet atmospheres. *ApJ* **632**, 1132–1139 (2005).
- [19] Agol, E. *et al.* The Climate of HD 189733b from Fourteen Transits and Eclipses Measured by Spitzer. *Astrophys. J.* **721**, 1861–1877 (2010).
- [20] Kislyakova, G., Kristina, Holmstrom, M., Lammer, H., Odert, P. & Khodachenko, M. L. Magnetic moment and plasma environment of hd209458b as determined from $ly\alpha$ observations. *Science* **346**, 981–983 (2014).
- [21] Gough, D. O. The Anelastic Approximation for Thermal Convection. *Journal of Atmospheric Sciences* **26**, 448–456 (1969).
- [22] Rogers, T. M. & Glatzmaier, G. A. Penetrative Convection within the Anelastic Approximation. *Astrophys. J.* **620**, 432 (2005).
- [23] Rauscher, E. & Menou, K. Three-dimensional Atmospheric Circulation Models of HD 189733b and HD 209458b with Consistent Magnetic Drag and Ohmic Dissipation. *Astrophys. J.* **764**, 103 (2013).
- [24] Lodders, K. Solar system abundances of the elements. *Principles and Perspectives in Cosmochemistry* (2010).
- [25] Iro, N., Bézard, B. & Guillot, T. A time-dependent radiative model of HD 209458b. *Astron. Astrophys.* **436**, 719–727 (2005).
- [26] Rogers, T. M. & Showman, A. P. Magnetohydrodynamic Simulations of the Atmosphere of HD 209458b. *Astrophys. J. Lett.* **782**, L4 (2014).